Bo Qing[1]
Department of Biological Engineering,
MIT,
Cambridge, MA 02139

Elizabeth P. Canovic[1]
Department of Materials Science
and Engineering,
MIT,
Cambridge, MA 02139

Aleksandar S. Mijailovic[1]
Department of Mechanical Engineering,
MIT,
Cambridge, MA 02139

Anna Jagielska
Department of Materials Science
and Engineering,
MIT,
Cambridge, MA 02139

Matthew J. Whitfield
Department of Materials Science
and Engineering,
MIT,
Cambridge, MA 02139

Alexis L. Lowe
Department of Neuroscience,
Wellesley College,
Wellesley, MA 02481

Elyza H. Kelly
Department of Neurology,
The F.M. Kirby Neurobiology Center,
Harvard Medical School,
Boston Children's Hospital,
Boston, MA 02115

Daria Turner
Department of Neurology,
The F.M. Kirby Neurobiology Center,
Harvard Medical School,
Boston Children's Hospital,
Boston, MA 02115

Mustafa Sahin
Department of Neurology,
The F.M. Kirby Neurobiology Center,
Harvard Medical School,
Boston Children's Hospital,
Boston, MA 02115

Krystyn J. Van Vliet[2]
Department of Biological Engineering,
MIT,
Cambridge, MA 02139;
Department of Materials Science
and Engineering,
MIT,
Cambridge, MA 02139
e-mail: krystyn@mit.edu

Probing Mechanical Properties of Brain in a Tuberous Sclerosis Model of Autism

Causes of autism spectrum disorders (ASD) are understood poorly, making diagnosis and treatment challenging. While many studies have investigated the biochemical and genetic aspects of ASD, whether and how mechanical characteristics of the autistic brain can modulate neuronal connectivity and cognition in ASD are unknown. Previously, it has been shown that ASD brains are characterized by abnormal white matter and disorganized neuronal connectivity; we hypothesized that these significant cellular-level structural changes may translate to changes in the mechanical properties of the autistic brain or regions therein. Here, we focused on tuberous sclerosis complex (TSC), a genetic disorder with a high penetrance of ASD. We investigated mechanical differences between murine brains obtained from control and TSC cohorts at various deformation length- and time-scales. At the microscale, we conducted creep-compliance and stress relaxation experiments using atomic force microscope(AFM)-enabled indentation. At the mesoscale, we conducted impact indentation using a pendulum-based instrumented indenter to extract mechanical energy dissipation metrics. At the macroscale, we used oscillatory shear rheology to quantify the frequency-dependent shear moduli. Despite significant changes in the cellular organization of TSC brain tissue, we found no corresponding changes in the quantified mechanical properties at every length- and time-scale explored. This investigation of the mechanical characteristics of the brain has broadened our understanding of causes and markers of TSC/ASD, while raising questions about whether any mechanical differences can be detected in other animal models of ASD or other disease models that also feature abnormal brain structure. [DOI: 10.1115/1.4040945]

Keywords: tuberous sclerosis, atomic force microscope-enabled indentation, impact indentation, rheology, brain, tissue mechanics

---

[1] B. Qing, E. P. Canovic, and A. S. Mijailovic authors contributed equally.
[2] Corresponding author.

Manuscript received November 28, 2017; final manuscript received July 12, 2018; published online January 18, 2019. Assoc. Editor: Barclay Morrison.

1 Introduction

Tuberous sclerosis complex (TSC) is a multisystem disease that includes multiple neurological symptoms. Approximately 50% of TSC patients also present autism spectrum disorders (ASD) [1,2]. Because of this co-occurrence, mice with TSC are used as animal models for autism studies [3]. TSC is caused by mutations in the *TSC*1 and *TSC*2 genes and the resulting loss of function of the encoded proteins, hamartin (TSC1), and tuberin (TSC2), which play critical roles in protein synthesis and cell growth control [1]. Using *Tsc*1/2 gene-deficient mouse models, researchers have identified defects in axonal formation, guidance, and myelination. Specifically, they have shown that loss of TSC function leads to neurons with abnormal axon morphology, hypomyelination, and hyperactivation of the mTOR pathway resulting in increased protein synthesis and cell growth [4–7]. Hypomyelination, characterized by reduced amounts of myelin ensheathing neuronal axons, is especially apparent in the corpus callosum and the radiating fibers extending into the cerebral cortex [4]. Similar defects in axonal organization and hypomyelination have also been found in TSC patients using diffusion tensor imaging [8–10]. While previous work has focused on the genetic and biochemical parameters contributing to the neurological symptoms in TSC/ASD patients, the physical factors that may affect brain pathology have not yet been investigated thoroughly, and represent an appealing new area of exploration for therapeutic and diagnostic applications in TSC/ASD and other neurological disorders affecting brain structure. Here, we investigate the relationship between the structural changes in TSC and the mechanical properties of the murine brain tissue at multiple length and time scales of deformation.

Structurally, brain tissue architecture is complex and hierarchical, with interlinked gray and white matter regions that differ in function and in cellular organization. Mechanically, brain is exceptionally compliant compared to other biological tissues, with elastic moduli E on the order of hundreds of Pascals [11], and can exhibit nonlinear and time-dependent viscoelastic deformation in response to applied deformations or loads. In other areas of the body, tissue structure and mechanical properties are altered in diseases including cancer, atherosclerosis, and asthma [12]. Recently, several groups have shown changes in brain mechanical properties during pathological conditions, such as Alzheimer's [13], multiple sclerosis [14], and encephalomyelitis [15]. Because of the major structural changes observed in TSC brains, we hypothesized the potential for corresponding changes in mechanical properties. Better understanding of the mechanical characteristics of the brain during pathology may suggest new treatment targets or diagnostic markers.

To consider such mechanical differences, we characterized the mechanical properties of TSC brain tissue with three different methods used to probe the brain at the micro-, meso-, and macrolength scales. At the microscale, we conducted atomic force microscope (AFM)-enabled indentation experiments to quantify the stiffness of the tissue, and subsequently of isolated neurons. While AFM-enabled indentation is typically used to estimate the elastic modulus of a sample [16–18], it is also effective at measuring time- or rate-dependent viscoelastic properties, including creep compliance and relaxation moduli [19–24]. At the mesoscale, we conducted impact indentation experiments using a pendulum-based instrumented nanoindenter to quantify relative energy dissipation metrics. From the damped harmonic oscillatory motion of a probe impacted into the tissue, we determined the mechanical energy dissipation capacity. Finally, at the macroscale, we employed parallel plate rheometry to quantify the frequency-dependent shear storage and loss moduli of the tissue. While we note and discuss that each of these methods includes assumptions, advantages, and challenges to mechanical characterization of murine brain tissue at different length scales and deformation rates, our goal was to identify any detectable differences between TSC brain tissue and wild-type cohorts in an established mouse model of ASD. There remain important distinctions and outstanding questions for such analyses in human brain tissue, and for other studies that seek to maximize the accuracy of any measured mechanical property of brain tissue rather than to identify robust relative mechanical comparisons between cohorts that are known to exhibit distinct structural or functional differences.

2 Materials and Methods

2.1 Tissue Sourcing. As described previously [4], mouse experiments were conducted in a mixed strain background (129S4/SvJae, C57BL/6, and CBA) but have been maintained as an inbred population in our colony for >7 years. Mice exhibiting the *SynI-cre* allele were a generous gift from Dr. Jamey Marth (University of California, San Diego, La Jolla, CA) [25]. The mice used in this study were generated through breeding between $Tsc1^{cc}$ females and either $Tsc1^{w\text{-}}$*SynI-cre*$^{+}$ or $Tsc1^{w\text{-}}$*SynI-cre*$^{++}$ males or between $Tsc1^{cc}$ males and $Tsc1^{cw}$*SynI-cre*$^{+}$ females. The symbols *c*, *w*, and - denote the conditional (floxed), wild-type, and null alleles of *Tsc1*, respectively. The *c* allele is referred to formally as $Tsc1^{tm1Djk}$. Mice were anesthetized at postnatal day 21 using ketamine (AnaSed Injections). Whole brains were removed, sliced if necessary, and immediately stored in round-bottomed tubes with Hibernate®-A media on ice. Tissue samples from 29 control and 22 TSC mice were used for subsequent mechanical characterization. All mechanical measurements were performed within 48 h postmortem. All procedures were performed in accordance with the *Guide for the Humane Use and Care of Laboratory Animals*, and the Animal Care and Use Committee of Boston Children's Hospital approved this study (IACUC approval 15-06-2955R).

2.2 Atomic Force Microscope-Enabled Indentation. All AFM-enabled indentation measurements were performed on an MFP-3D atomic force microscope (Asylum Research, Oxford Instruments, Abingdon, UK) using a silicon-nitride cantilever with a nominal spring constant of 0.03 N/m and an attached 20 μm diameter borosilicate bead (Novascan; lowest cantilever stiffness available for that probe geometry). The brain tissue was sectioned into coronal slices of 350 μm thickness, and mounted in a polystyrene dish using Cell-Tak (Corning). The corpus callosum of the tissue was probed in order to measure the mechanical properties of white matter. While axonal tracts in the white matter are aligned such that the tissue structure is anisotropic, and thus the elastic properties are also expected reasonably to vary with orientation or texture [26,27], we assumed elastic isotropy as a first approximation. Structural anisotropy can affect indentation response, though generally plastic anisotropy is more pronounced than elastic isotropy [28]. We also maintained the relative orientation of the brain slices with respect to the indentation direction for the control and TSC cohorts, facilitating comparisons between these two sample groups. Measurements were conducted on tissue fully immersed in Hibernate®-A media, and temperature was maintained at 37 °C.

Young's elastic modulus. For each tissue sample, force versus depth responses (F–δ) was obtained. Samples were indented nominally to a depth of 4 μm at an indentation velocity of 4 μm/s, which were maximum depths and velocities similar to those in previous AFM mechanical studies on brain tissue [29,30]. From the F–δ response, the contact point was determined using an algorithm described by Lin et al. [31]. Elastic modulus E was calculated according to the model derived by Oliver and Pharr for an incompressible material indented with a spherical probe of radius $R = 10$ μm [32,33]. Herbert et al. previously detailed the application of the Oliver–Pharr model for a spherical indenter [33]. While these conditions and depths were comparable to other reports that adopted a linear elastic deformation assumption [29], we note that the maximum effective strains we applied (~12%, estimated as $0.2a/R$ where a is the contact radius at the maximum indentation depth) exceeded the approximate strains of ~1% beyond which this linear elastic assumption is well supported. Nevertheless, our use of this idealization facilitated comparison between cohorts. This model, which analyzes the unloading response, was chosen over the more frequently used Hertz model to account for inelastic deformation of the sample, as demonstrated by the hysteresis between the approach and the retract curves from the force versus depth responses. A power law function was fit to the portion of the unloading curve from 10 to 95% of the peak or maximum force. The slope of the unloading curve was then calculated as the derivative of the fitted power law function at 95% of the peak force. Tissue slices from 12 control and ten TSC mice were examined by at least ten indentations, each at different locations, per animal.

Creep compliance. The tissue was indented to a set force, and deformation was measured over time as it increased. Indentation depth versus time responses (δ–t) were obtained in the corpus callosum. Idealizing the tissue as incompressible, creep compliance $J_C(t)$ was calculated from the solution derived by Lee and Radok [34]

$$J_C(t) = \frac{16\sqrt{R}}{3F_0}\delta^{3/2}(t) \tag{1}$$

The maximum applied force F_0 was nominally 5 nN, though the exact applied force was determined by the product of the calculated cantilever stiffness and deflection. The time required to ramp to this set force was approximately 0.5 s. $J_C(t)$ was fit to a standard linear solid (SLS) spring-dashpot model (spring in parallel with a Maxwell element) to obtain the long-term equilibrium shear modulus G_∞, short-term instantaneous shear modulus G_0, and creep relaxation time τ_c

$$J_C(t) = \frac{1}{G_\infty} - \left(\frac{G_0 - G_\infty}{G_0 G_\infty}\right)e^{-\frac{t}{\tau_c}} \tag{2}$$

Stress relaxation. The tissue was indented to a specified cantilever base displacement corresponding to a maximum measured indentation depth, and force was measured as it decreased or relaxed over time. Force versus time responses (F–t) were obtained in the corpus callosum, with a nominal indentation depth $\delta_0 = 3$ μm. The time needed to reach this set displacement was approximately 0.2 s. Shear relaxation modulus $G_R(t)$ was calculated using the solution derived by Lee and Radok [34]

$$G_R(t) = \frac{3}{16\sqrt{R}\delta_0^{3/2}}F(t) \tag{3}$$

$G_R(t)$ was also fit to the standard linear solid model to obtain viscoelastic moduli and the relaxation time τ_r

$$G_R(t) = G_\infty + (G_0 - G_\infty)e^{-\frac{t}{\tau_r}} \tag{4}$$

The creep relaxation time τ_c can be related to the relaxation time τ_r by

$$\tau_r = \frac{G_\infty}{G_0}\tau_c \tag{5}$$

Converting G to E. By only assuming that the material is linear viscoelastic and isotropic, Lakes et al. have demonstrated that the shear relaxation function $G(t)$ and Young's relaxation function $E(t)$ may be related in the frequency domain by

$$\overline{E}(s) = 2\overline{G}(s)(1 + s\overline{\nu}(s)) \tag{6}$$

where $\overline{E}(s)$, $\overline{G}(s)$, and $\overline{\nu}(s)$ are the Laplace transformed Young's relaxation function, shear relaxation function, and Poisson's ratio, respectively; s is complex frequency [35]. If $\overline{\nu}(s)$ is assumed to be constant and incompressible ($\nu = 0.5$), as is assumed frequently for hydrated biological soft tissues [36–38], Eq. (6) may be rewritten in the time domain as

$$E(t) = 2G(t)(1 + \nu) = 3G(t) \tag{7}$$

We adopted those same simplifications and assumptions for brain tissue deformation, to enable comparison between control and TSC cohorts. It follows that the equilibrium Young's modulus E_∞ and instantaneous Young's modulus E_0 are

$$E_\infty = 3G_\infty \tag{8}$$

$$E_0 = 3G_0 \tag{9}$$

Statistical analysis. To determine whether the mechanical properties of control brain tissue differed statistically from that of TSC brain tissue, a series of Mann–Whitney U-tests were conducted for each measured parameter. The Mann–Whitney U-test is a nonparametric test applied to independent samples and does not require the assumption of normal distributions. Our criterion for significance was $p < 0.01$, which was a conservative threshold also adopted by previous comparative studies on brain tissue mechanical properties that identified a statistically significant difference between cohorts [39–42].

2.3 Impact Indentation. Impact indentation experiments were conducted on all brain tissues at 25 °C via a pendulum-based instrumented nanoindenter (Micro Materials Ltd. NanoTest Vantage, Wrexham, UK). Unlike AFM-enabled indentation, the impact indentation setup did not enable testing in fluids at physiological temperature. As described in our previous work [43,44], this technique monitors the probe displacement over time as the pendulum swings into the sample at the desired impact velocity. Impact velocity is a parameter that is controlled in open-loop format, as the driving force to hold the pendulum stationary prior to release and impact is the parameter that is controlled in closed-loop feedback. Thus, the applied impact velocity can be affected by various other factors related to the calibration procedure. Since the brain tissue samples were collected periodically over an extended period of time, the experimental setup was reconfigured and recalibrated several times, which led to slightly different impact velocities for the same requested driving force. The displacement profile was analyzed using customized MATLAB scripts to compute the maximum penetration depth, energy dissipation capacity, and energy dissipation rate. Here, a stainless steel cylindrical flat punch with a radius of 1 mm was used to probe each sample. Whole mouse brains were sliced into sections of 6 mm thickness along the sagittal direction and adhered to the sample post using a thin layer of low-viscosity cyanoacrylate adhesive (Loctite® 4013). As the probe diameter was relatively large compared to the dimensions of the brain sample (Fig. S1, which is available as Supplemental Material on the ASME Digital Collection), we selected measurement positions near the center of the sample to both standardize and minimize artifacts of the finite sample dimensions (edge effects); these measurement positions were within 1–2 mm from the tissue perimeter. This distance was similar to the probe contact radius such that it was conceivable that the free surface or edges affected the accuracy of inferred impact response properties. However, the sample dimensions were maintained constant between the control and TSC brain tissues such that comparisons between the two groups remained sound. Similarly, potential artifacts attributable to finite sample thickness and the potential for mechanical contributions from the underlying substrate [36,45] existed and were recognized, but were also maintained similar among samples and between cohorts. Brain tissues were immersed fully in Hibernate®-A media during mechanical characterization under impact loading, as described originally for fluid-immersed samples [46]. Applied impact velocities ranged from 2 to 5 mm/s, corresponding to strain energy densities on the order of 1 kJ/m^3. A total of six control and four TSC brains were characterized, and at least three impact measurements were obtained for each brain.

2.4 Oscillatory Shear Rheology. Rheological experiments were conducted using a parallel plate rheometer (MCR 501, Anton-Paar, Graz, Austria) at 25 °C with a plate diameter of 10 mm and a torque limit of 0.5 μN m. Measurements were conducted on coronal brain slices of 1 mm thickness. A total of seven control and five TSC brains were characterized. Sandpaper (320 grit, McMaster Carr) was adhered to the top and bottom rheometer plates to minimize slip between the plates and brain tissue. Contact between the top measurement plate and brain tissue was determined to have occurred when the force transducer maintained a normal force of 0.01 N after a relaxation period of 5 min. After contact, the tissue was hydrated using Hibernate®-A media, and a hood was placed over the sample to minimize evaporation. Amplitude sweeps were conducted at 1 and 10 rad/s, and the linear viscoelastic limit was measured to be approximately 1–3% shear strain. Frequency sweeps were performed at 1% shear strain in the frequency range of 0.1–40 rad/s. Shear storage moduli G' and loss moduli G'' were calculated as a function of frequency via software within the Anton-Paar instrument using the radius of the plate R, height of the sample L, amplitude of the applied angular displacement ϕ_0, measured torque T_0, and phase lag φ

$$G' = \frac{2L}{\pi R^4}\frac{T_0}{\phi_0}\cos\varphi \tag{10}$$

$$G'' = \frac{2L}{\pi R^4}\frac{T_0}{\phi_0}\sin\varphi \tag{11}$$

The measured G' and G'' at different frequencies can be converted to a Prony series

$$G'(\omega) = G_\infty + \sum_{j=1}^{N}\frac{G_j\omega^2\tau_j^2}{1+\omega^2\tau_j^2} \tag{12}$$

$$G''(\omega) = \sum_{j=1}^{N}\frac{G_j\omega\tau_j}{1+\omega^2\tau_j^2} \tag{13}$$

where ω is the frequency, N is the number of Maxwell elements, and G_j and τ_j are the elastic components and relaxation times associated with the Maxwell elements, such that

$$G_0 = G_\infty + \sum_{j=1}^{N} G_j \tag{14}$$

A constrained nonlinear least-squares optimization scheme in MATLAB was used to determine the number of Maxwell elements needed to produce a good fit to the rheological data. G_∞ and G_0 can be converted to E_∞ and E_0 as mentioned previously.

2.5 Immunohistochemical Fluorescent Staining. Mouse brains were sectioned into coronal slices. Next, these coronal brain sections were fixed using paraformaldehyde and mounted onto glass slides. After washing in 150 mM NaCl phosphate-buffered saline (PBS), slides containing the fixed brain sections were incubated in blocking buffer (0.5% Triton™ X-100 and 10% goat serum in PBS) for 30 min. Image-iT® FX signal enhancer was used to cover the slices for 30 min to mitigate nonspecific fluorescence. Sections were incubated with a rabbit polyclonal antibody to fibronectin (Millipore, AB2033) diluted 1:100 in blocking buffer overnight at 4 °C. After washing in PBS, sections were incubated with secondary antibody (Alexa Fluor® 594-conjugated goat anti-rabbit) diluted 1:500 and with Hoescht® 33,342 diluted 1:10,000 in PBS for 2 h. Sections were washed again in PBS and after drying, and slides were mounted and visualized with a fluorescent microscope (Olympus IX51 equipped with Haramatsu Orca ER CCD camera). Using ImageJ, the entire area within each brain slice was selected as the region of interest for quantification of fibronectin expression. For each slice, the mean fluorescence intensity was calculated by first dividing the integrated density value by the area of the region of interest and then subtracting the mean intensity of background readings. We note that these tissue slices used for immunohistochemical analysis were not the same slices that were characterized mechanically. Detaching these fragile samples after adhesion to rigid supports for mechanical tests compromises structural integrity. Additionally, the same tissue slices could not be stained and imaged prior to mechanical testing because chemical fixation of the samples would affect the mechanical properties.

3 Results

3.1 Microscale Mechanical Properties. Using AFM-enabled indentation, we probed microscale volumes comparable to cell sizes, and characterized the mechanical properties of brain tissues from healthy control mice and TSC mice as shown in Fig. 1. AFM provided high spatial resolution to enable local measurements of white matter-rich regions, such as the corpus callosum (Fig. 1(*a*)). We were interested primarily in the corpus callosum because this region contains the highest concentration of myelinated axons.

Since we sought to identify any mechanical changes caused by the TSC mutation, we first idealized brain tissue as a linear elastic material, and used the Oliver–Pharr analysis to quantify the Young's elastic moduli E for each tissue sample. Examples of typical force–displacement responses for both control and TSC groups are shown in Fig. S2, which is available as Supplemental Material on the ASME Digital Collection. Although this assumption of brain tissue deforming linear elastically is an idealization and imperfect assumption for the strains applied in this study (see Sec. 2 and [47,48]), this enabling simplification facilitated comparison between the effective E of the control and TSC cohorts, and specifically the identification of any detectable and statistically significant differences between those cohorts. We measured the mean E to be 381 Pa for control white matter and 348 Pa for TSC white matter (Fig. 1(*b*)). However, we identified no statistically significant differences between the elastic moduli of control and TSC brain tissue.

Next, we treated brain tissue as a linear viscoelastic material to explore for potential differences in time-dependent behavior. To characterize the microscale viscoelastic properties, we conducted both creep compliance and stress relaxation experiments. From the creep and stress relaxation response, we calculated the equilibrium modulus E_∞ (Fig. 1(*c*)), instantaneous modulus E_0 (Fig. 1(*d*)), and relaxation time τ_r (Fig. 1(*e*)) by assuming a standard linear solid model (see Sec. 2 and Eqs. (1)–(4)). The fits matched well to our creep compliance and stress relaxation response (Fig. S3, which is available as Supplemental Material on the ASME Digital Collection), with R^2 values exceeding 0.93 and 0.85, respectively. We note that the measured values of E_0 and τ_R are not as robust as the values of E_∞ because ideal instantaneous steps of applied load or displacement cannot be achieved experimentally, and thus short timescale information is lost during the ramp period. Nonetheless, we can still compare the relative values of these properties between the two cohorts since the loading conditions were maintained the same. We did not observe statistically significant differences in any of these viscoelastic properties between control and TSC brain tissue. Comparing the creep compliance results to the stress relaxation results, we found E_∞ and E_0 were similar in magnitudes for each sample group. However, the relaxation time constants measured via stress relaxation were higher than those measured via creep likely because the ramp time to achieve a "step" was longer in creep than in stress relaxation. A longer ramp time provides the material more time to relax.

3.2 Mesoscale Mechanical Properties. At the mesoscale or intermediate deformation length scales, we conducted impact indentation using a 1 mm radius cylindrical flat punch probe, quantifying the tissue's energy dissipation response to loading representative of some traumatic injuries [43]. The measured maximum penetration depth $x_{\max}$ (Fig. 2(*a*)), unitless energy dissipation capacity K (Fig. 2(*b*)), and unitless dissipation quality factor Q (Fig. 2(*c*)) are shown as a function of impact velocity, allowing investigation of these deformation rate-dependent properties of brain tissue. A larger magnitude of $x_{\max}$, K, and Q corresponds to a lower resistance to deformation, a greater extent of impact energy dissipation during the first impact cycle, and a lower energy dissipation rate, respectively. All three parameters depended on impact velocity: $x_{\max}$ and K increased, while Q decreased with increasing impact velocity. These trends are consistent with those reported previously by impact loading studies on other soft tissues obtained from heart and liver [43,49]. When comparing the control and TSC brains, we observed no statistically significant differences for each of the impact response parameters considered, within the ranges of loading conditions studied here. For example, at the lowest impact velocity, control brain tissue exhibited $x_{\max}$ of 0.428 ± 0.035 (mean ± standard deviation), K of 0.640 ± 0.101, and Q of 1.443 ± 0.202, while TSC brain tissue exhibited an $x_{\max}$ of 0.378 ± 0.072 (mean ± standard deviation), K of 0.701 ± 0.137, and Q of 1.571 ± 0.160.

3.3 Macroscale Mechanical Properties. At the macroscale or deformation of entire brain tissue sections, we used oscillatory

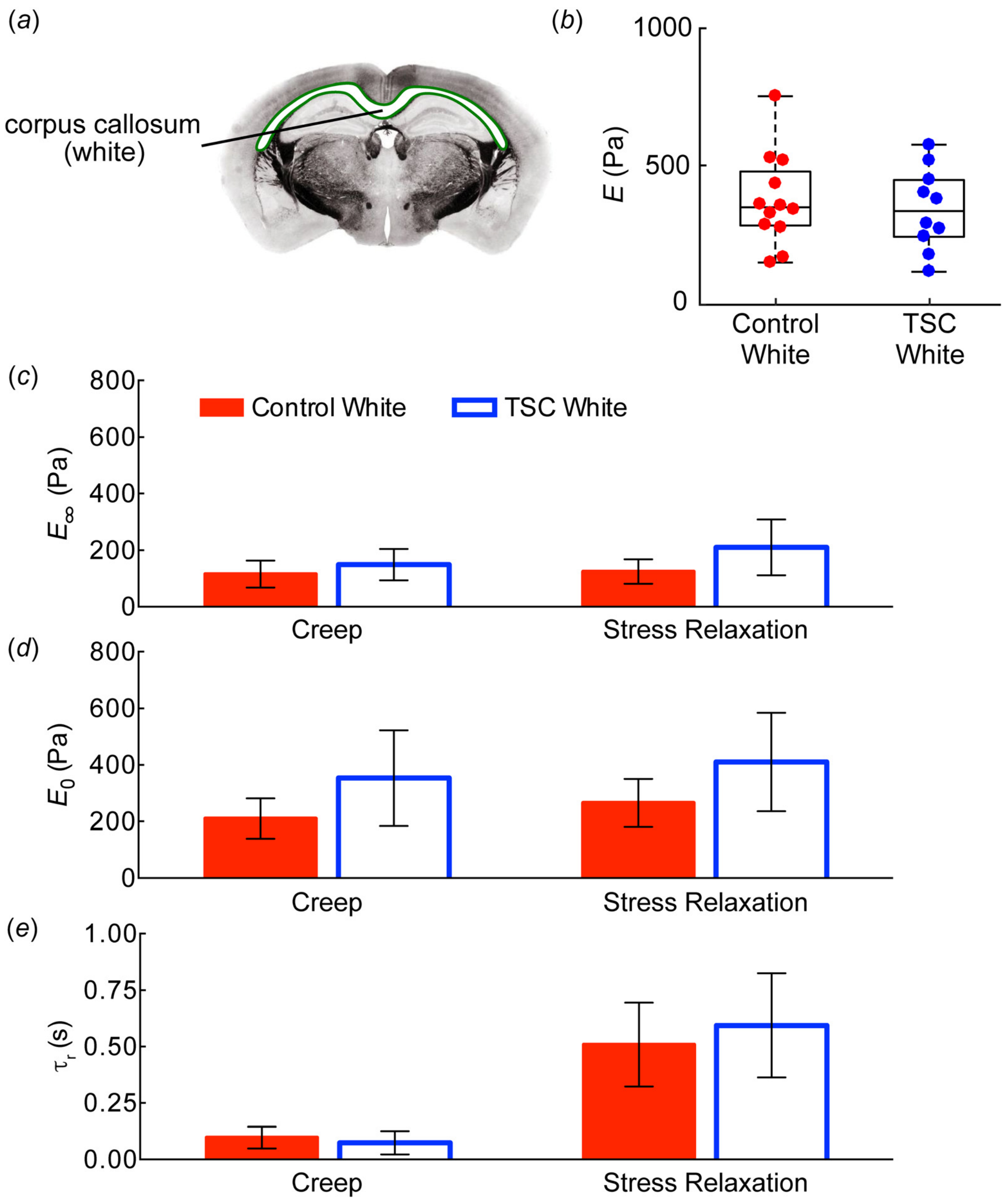

Fig. 1 Mechanical properties at the micrometer length scale measured using AFM-enabled indentation in the white matter of healthy control and TSC mice: (*a*) schematic of a coronal section of mouse brain indicating the location of the corpus callosum, (*b*) the Young's elastic modulus E of TSC brain tissue is not significantly different than that of control tissue, (*c*) equilibrium modulus E_∞, (*d*) instantaneous modulus E_0, and (*e*) relaxation time τ_r obtained from fitting creep (left) and stress relaxation (right) data with a SLS model. These experiments also show no significant differences in any viscoelastic property between the control and TSC brains. Data are represented as mean ± standard deviation ($n > 10$ measurements per animal; each data point in Fig. 1(*b*) represents an animal; in Figs. 1(*c*)–1(*e*), four control and three TSC animals were characterized for creep and stress relaxation experiments).

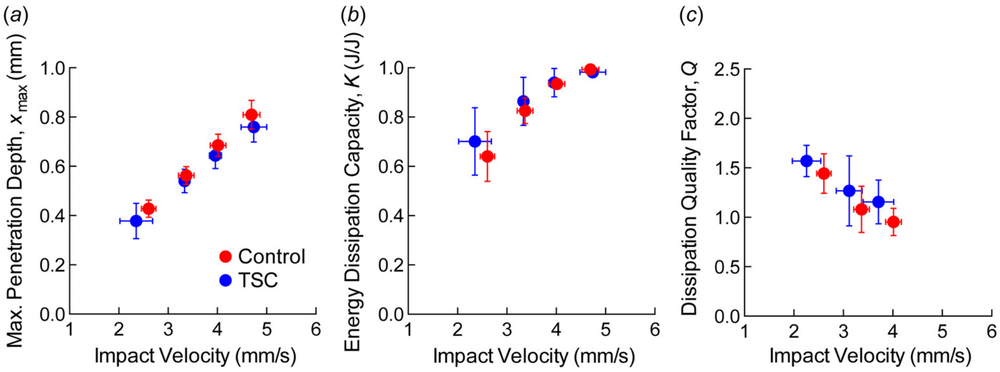

Fig. 2 Impact energy dissipation response metrics of control and TSC mouse brain tissue. (*a*) maximum penetration depth x_{max}, (*b*) energy dissipation capacity *K*, and (*c*) dissipation quality factor *Q* obtained at different impact velocities show no statistical difference between control and TSC brain tissue. Data are represented as mean ± standard deviation ($n > 3$ measurements per animal; six control and four TSC animals were characterized).

shear rheology to quantify the frequency-dependent shear storage modulus G' and loss modulus G'' of the tissue. Figure 3 shows G' and G'' for frequencies ranging from 0.1 rad/s to 40 rad/s. We measured the mean G' to range from 141 Pa (at 0.1 rad/s) to 576 Pa (at 40 rad/s), and mean G'' to range from 27 Pa (at 0.1 rad/s) to 109 Pa (at 40 rad/s) for the control tissues. For the TSC tissues, we found the mean G' to range from 132 Pa (at 0.1 rad/s) to 530 Pa (at 40 rad/s) and mean G'' to range from 28 Pa (at 0.1 rad/s) to 118 Pa (at 40 rad/s). The magnitudes of G' and G'' of all brain tissues increased monotonically with increasing oscillation frequency within the ranges studied herein. While the magnitude and trend of G' and G'' agree well with previous studies in healthy murine and porcine brain tissue that examined a similar frequency range [47,50,51], we identified no significant differences in these macroscale, dynamic shear moduli as a function of disease state (i.e., control versus TSC). These findings are consistent with our results at the micro- and mesolength scales.

3.4 Fibronectin Matrix Comparison. Given that we identified no statistically significant differences in tissue mechanical properties between healthy control and TSC brain, we sought to explore whether the extracellular matrix (ECM) was also similar in these tissues. Using fluorescent immunohistochemistry, we stained brain tissues for fibronectin, a component of the ECM, because increased fibronectin expression in the brain has been associated with demyelination diseases and changes in tissue stiffness [52–54]. Additionally, changes in fibronectin expression by cultured fibroblasts from skin lesions of patients with TSC have been observed previously [55]. Figures 4(*a*) and 4(*b*) show representative images of the fibronectin stain for control and TSC brain slices, respectively. The expression level of fibronectin was relatively low for brain tissue, as expected from previous immunohistochemical reports, and thus we rendered the images (increased brightness and contrast) in Figs. 4(*a*) and 4(*b*) equally for visualization purposes [52]. Figure 4(*c*) quantifies the intensity of the red fluorescence in the original images for every stained tissue

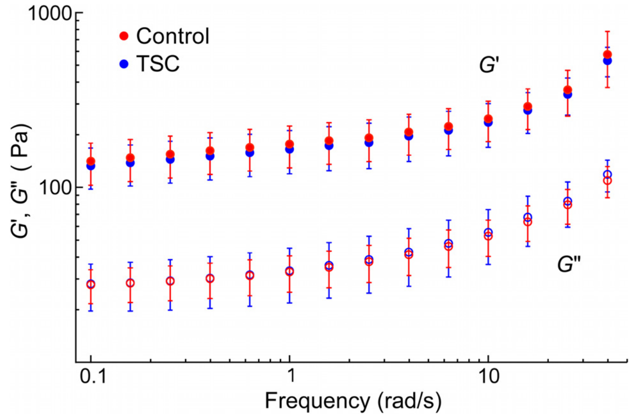

Fig. 3 Storage G' moduli (filled symbols) and loss G'' moduli (open symbols) of control and TSC brain tissue at a range of frequencies. Both G' and G'' show no statistical difference between control and TSC brain tissue for all frequencies measured here. Data are represented as mean ± standard deviation ($n = 7$ control and 5 TSC mouse brains).

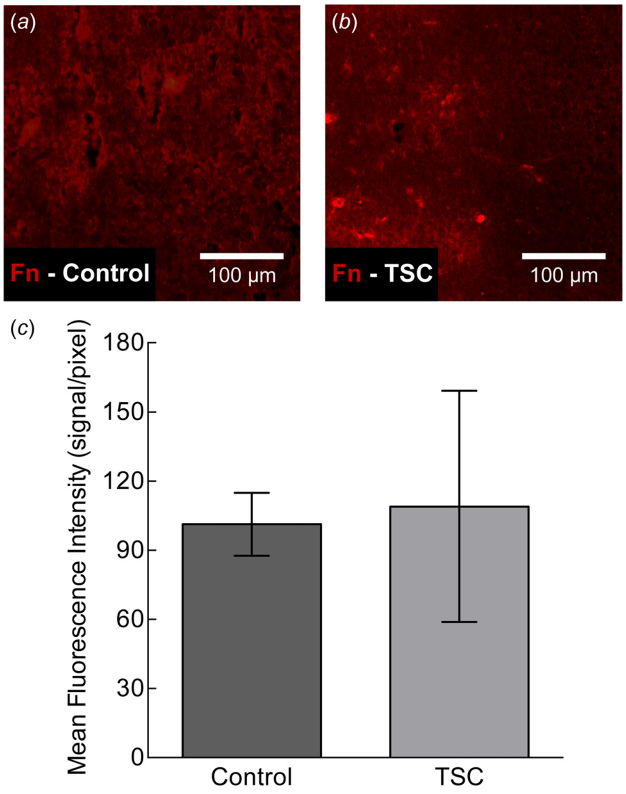

Fig. 4 Representative images of (*a*) control and (*b*) TSC coronal brain slices analyzed for the expression of fibronectin protein (Fn) using fluorescent immunohistochemistry. (*c*) Mean fluorescence intensity quantified in the original images shows no statistical difference between control and TSC slices. Data are represented as mean ± standard deviation ($n = 4$ control and five TSC slices).

slice and compares the two cohorts. We observed no significant difference in signal intensity between control and TSC slices, but noted higher standard deviation of the intensity for the TSC group. The similar degree of fibronectin expression between the two groups is consistent with our statistically indistinguishable mechanical characterization results between these two cohorts of control and TSC mice.

4 Discussion

4.1 Effects of Brain Structure on Tissue Mechanical Properties. The goal of this study was to identify any detectable and statistically significant differences in mechanical response between control and TSC brain tissue—under the simplifying assumptions and limitations of several methods distinguished by different deformation length and time scales—given that the TSC/ASD condition is associated with optically detectable changes in tissue structural features such as demyelination that have been correlated with changes in animal functional behavior. The most striking evidence for demyelination altering properties correlated with tissue mechanics is from a recent study by Schregel et al. These authors showed that chemically induced demyelination in mouse brain was associated with a reduction in signals generally correlated with mouse brain tissue stiffness as measured by magnetic resonance elastography (MRE) [54]. Moreover, they showed that the mechanical changes were reversible, as remyelination led to a restoration of MRE signals correlated with stiffness. However, the copper-chelator cuprizone that was used to induce demyelination in that study also resulted in a number of other changes in brain physiology. These induced changes included degradation of ECM density and homogeneity, upregulation of glycosaminoglycans and fibronectin, increased glial cell populations, and increased beta-amyloid precursor protein in axons. It is unclear which of those parameters contributed to the decrease in the complex shear modulus inferred from MRE. Thus, although chemically induced demyelination led to detectable changes in a mechanical parameter, that study did not intend to show or claim that a different demyelinating condition such as TSC would result in similar structural or mechanical changes. Even more recently, Weickenmeier et al. used nanoindentation experiments in combination with histological staining to examine the relationship between brain stiffness and myelin content in prenatal and postnatal bovine brains. Those authors found that white matter stiffness and myelin content exhibited a strong Pearson correlation coefficient above 0.90, as both significantly increased upon tissue maturation in the brains that they studied [41,56].

In the present study, we explored whether a similar relationship between tissue stiffness and tissue structure could be identified in our genetic mouse model of TSC/ASD. We characterized the mechanical properties over a range of length scales, spanning the microscale via AFM-enabled indentation, mesoscale via impact indentation, and macroscale via oscillatory shear rheology. Table 1 summarizes our key results, providing a comprehensive list of moduli as determined by the various approaches we employed. The magnitudes of these measured moduli were dependent on the technique used and the corresponding assumptions. Indeed, each approach included assumptions regarding material constitutive laws and contact mechanics that relate to the accuracy of a reported mechanical property, but these practical constraints were maintained constant between the control and TSC cohorts to enable comparisons. A series of Mann–Whitney tests were conducted for each parameter to compare the two tissue groups (significance at $p < 0.01$). We note that this significance threshold was also used by previous studies of similar sample size and methods, which detected differences in mechanical properties as a function of age, species, and/or region within the brain tissue [39–42]. Together, the results in Table 1 demonstrate that despite exploring multiple length and time scales, we found no statistically significant differences when comparing healthy control and TSC brain tissue. Ultimately, the lack of detectable differences over a broad array of methods and scales suggests that the structural changes associated with this genetic defect do not correspond to significant changes in the brain mechanical properties quantified herein.

One of the most notable differences in TSC brain structure is the significant reduction of myelinated axons. Since white matter contains the highest concentration of axons, we hypothesized that the corpus callosum would exhibit the most pronounced differences in mechanical properties. Murine brain contains only roughly 10% white matter such that the corpus callosum constitutes a very low percentage of the total sample volume [57]. Thus, AFM-enabled indentation was the only technique of those considered herein that could distinguish reliably between white and gray matter and measure to detect potential differences in local elastic and viscoelastic properties. However, as shown in Fig. 1, we found that the Young's elastic modulus and the viscoelastic mechanical properties (E_∞, E_0, and τ_r) of white matter in TSC brain tissue did not differ significantly from that of white matter in our healthy control group. In this study, we considered only coronal brain sections using AFM-enabled indentation; other section orientations (in particular sagittal) require future exploration as they may exhibit different mechanical properties due to the structure and alignment of white matter tracts [58–61]. We also note that the age of these mice was 21 days, and it is possible that the mechanical properties of white matter in TSC and control brains will vary differently with developmental age. However, as is observed with this mouse model, the TSC cohort did not survive consistently beyond 21 days so we could not consider differences at later developmental stages.

Additionally, we did not discount the possibility that mechanical differences could be identified at larger length scales, because there is also pronounced demyelination in the murine TSC cortex [4] and potentially other structural differences associated with cellular and ECM organization. Therefore, we conducted spatially concentrated impact loading (impact indentation) and oscillatory shear rheology experiments on whole brain slices. For impact indentation, we observed no detectable differences in maximum penetration depth, energy dissipation capacity, and energy

Table 1 Moduli of healthy control and TSC brain tissue calculated using various techniques and assumptions. Data are represented as mean ± standard deviation ($n > 30$ measurements for AFM-related experiments; $n > 5$ measurements for shear rheology experiments). For each property, p value corresponds to Mann–Whitney comparisons between control and TSC cohorts, with statistical significance threshold of $p < 0.01$.

Moduli	Characterization method	Control brain tissue	TSC brain tissue	p value
Young's modulus E (Pa); elastic assumption	AFM-enabled indentation	381 ± 166	348 ± 148	0.125
Equilibrium modulus E_∞ (Pa); viscoelastic assumption	Creep via AFM	116 ± 48	150 ± 56	0.083
	Stress relaxation via AFM	125 ± 43	210 ± 98	0.058
	Oscillatory shear rheology	339 ± 100	306 ± 77	0.551
Instantaneous modulus E_0 (Pa); viscoelastic assumption	Creep via AFM	211 ± 71	353 ± 170	0.036
	Stress relaxation via AFM	265 ± 85	410 ± 175	0.074
	Oscillatory shear rheology	1064 ± 265	1057 ± 320	0.967

dissipation rate for all impact velocities examined here. Similarly, for rheology, we found no measurable differences in the magnitude and trend of dynamic shear moduli as a function of frequency, suggesting that both stiffness and viscous energy dissipation are similar between TSC and healthy brain tissue. Together, these results suggest that the differences in TSC axon structure, connectivity, and degree of myelination are not sufficient to elicit detectable changes in these mechanical properties.

To further understand how brain structure may affect mechanical properties, we also examined the ECM of our healthy control and TSC brain tissue. Although we were aware of the differences in axon structure and myelination levels, it was not established whether the composition and organization of the ECM were also detectably altered in this TSC model. Because brain tissue lacks the typical proportion of fibrillar collagen present in other tissues, it is generally believed that the mechanical properties and organization of neurons and glia are the key parameters responsible for the mechanical compliance of brain tissue [62]. The ECM is thought chiefly to provide topographical and biochemical cues to regulate cell behavior [54,62–65]. However, to our knowledge, there has been no direct experimental evidence to support such claims. In our study, we quantified the expression levels of fibronectin and found no significant alterations in TSC compared to control (Fig. 4). The similar amount of fibronectin expression is consistent with the hypothesis that the ECM in TSC brain remains similar to that of healthy cohorts, but future work is needed to quantify the levels and organization of other ECM constituents, including laminin, collagen IV, and various chondroitin sulfate proteoglycans. If the ECM is the same in TSC compared to control brain tissue, this structural similarity of the matrix can potentially explain the lack of differences in the tissue mechanical properties that we measured.

While there were no detectable differences between TSC and healthy brain tissue mechanics by the above analyses, our mechanical measurements on mouse brain tissue generally agree well with existing data for healthy brain tissue. Due to the difficulties associated with characterizing compliant materials and brain tissue's complex mechanical behavior caused by its nonlinear, viscoelastic, poroelastic, and anisotropic properties, previously reported measurements of linear viscoelastic moduli and elastic moduli have varied by orders of magnitude [66]. Our findings for the elastic moduli of mouse brain are consistent with previous work that have reported E to be on the order of hundreds of Pascals [67,68]. Furthermore, our shear rheology data exhibit similar magnitudes and trends compared to many previous studies reported for various animals, including mice, with weak power laws in G' and G'' as a function of frequency and a shear relaxation modulus on the order of hundreds of Pascals [51,59,66].

4.2 Cell-Level Mechanics of Individual Neurites.

Additionally, we considered whether the mechanical stiffness of individual neurites could differ for TSC cohorts. Detectable differences in axon stiffness, for example, could serve as a mechanical cue to the oligodendrocytes that engage and myelinate the axons, as those glial progenitor cells have been shown to exhibit mechanosensitive migration and differentiation in vitro [69]. To consider this possibility, we transfected neurons with the TSC vector and its empty vector control, and measured the elastic moduli of neurites from each cohort (see Supplementary Material on the ASME Digital Collection). We first used optical microscopy to carefully select the neurite that appeared the most elongated per cell body. These neurites were assumed to be axons and were mechanically characterized via AFM-enabled indentation.

The data in Fig. S4, which is available as Supplemental Material for this paper on the ASME Digital Collection are presented as stiffness normalized by the mean of the unmodified control cohort because the μm-scale diameter of the neurons conflated accurate measurement of the axon stiffness. However, qualitative comparison among these three groups of cells is sound, as the axon diameter was imaged and measured for each measurement and the relative deformation was maintained comparable among groups. While the *Tsc1* knockout axons were observed to be more compliant than the control or unmodified axons, there were no statistically significant differences between the stiffness of the *Tsc1* knockout axons and the stiffness of the axons from cells transfected with only the empty vector control. Thus, we cannot conclude that the control axons are stiffer, as the detectable changes in mechanical properties may also or instead be attributable to the transfection procedures. Future studies may consider other means to obtain and compare cell-level stiffness, including other means to transfect cells with appropriate control measurements or other approaches to isolate and maintain viable neurons from TSC cohorts.

4.3 Limitations of Mechanical Characterization Methods.

Each mechanical characterization technique utilized herein confers unique limitations and advantages, especially if probing highly compliant, anisotropic, nonlinear, and viscoelastic materials such as brain tissue. Strictly, each method includes assumptions of the material constitutive behavior (e.g., linear elastic or elastically isotropic), sample geometry (e.g., semi-infinite half-plane), and material microstructure (e.g., homogeneous). Additionally, each method employs instrumentation that varies in the instrument control loops for closed feedback control of applied load, applied displacement, or neither. Nevertheless, although the magnitude of mechanical properties reported herein includes the potential for inaccuracies due to limitations of each characterization technique, we emphasize that this study aimed to compare TSC to control brain tissue. Thus, experimental conditions were maintained constant when testing different tissue samples with a given method, to enable sound comparison between these two cohorts.

For AFM-enabled indentation, measurement accuracy in calculated elastic modulus is facilitated by choice of cantilever stiffness that is comparable to sample stiffness (if known) [70]; this is difficult to achieve for samples as compliant as brain tissue and for cantilevers of specific probe geometry such as μm-scale spheres. Additionally, when measuring the effective Young's elastic modulus with AFM-enabled indentation, time-dependent behaviors such as creep can occur during the unloading process, and will influence the measured force versus depth response. Thus, the stiffness quantified by the Oliver and Pharr method of indentation data analysis can be overestimated. Further, as outlined in Sec. 2, that analysis assumes a linear elastic constitutive response—an idealization that is more reasonably assumed at low applied strains and is an oversimplification at these indentation strains that we adopted to facilitate comparison between sample cohorts. We note that our AFM-indentation experiments were conducted to depths and at cantilever velocities comparable to that of other studies employing this method for brain tissue [29]. Additionally, the approximate strain rates (~0.5/s) in our present experiments were comparable to the strain rates that we calculated from others' AFM-based experiments (~0.5/s in Moeendarbary et al. [29]) and instrumented indenter-based experiments (~0.001/s–0.2/s in Budday et al. [42]) on brain tissue. Those studies also extracted the Young's elastic modulus by assuming a linear elastic response, and reported similar magnitudes as those in Fig. 1 and Table 1. Budday et al. also noted that the effective Young's elastic modulus of brain tissue increased with increased indentation velocity [42]. On the other hand, when we do consider the viscoelastic properties of brain tissue and conduct creep compliance or stress relaxation experiments, the experimentally applied force or indentation depth is not an ideal step function. Instead, the force or indentation depth is ramped to the desired value over short timescales. Since information at short time scales (i.e., time scales comparable to the ramp duration) will be lost during the ramp period, the measured values of instantaneous modulus and relaxation time are not as accurate as the values of equilibrium modulus [22]. Nonetheless, we can still compare the relative values of these properties between the two cohorts since the loading conditions were maintained the same.

At the mesoscale, impact indentation requires accurate detection of contact between the probe and tissue surface. As the sample approaches the probe, contact is detected when the pendulum is pushed back by the sample. However, for sufficiently compliant materials, the stationary probe can first deform the sample before enough force is applied to detectably deflect the pendulum. Thus, before the pendulum is ready to swing forward and impact the tissue, it is important to allow enough time for the tissue to restore and relax to its initial condition. Additionally, as mentioned in Sec. 2, the current impact indentation experimental design is limited to room temperature (25 °C). Future work can include modifications to the instrument to add temperature control capabilities that will enable characterization in fluid at constant, elevated temperatures of 37 °C. Finally, at the macroscale, accurate contact detection is also an important consideration for shear rheology experiments. Compressive axial strain can be appreciable even with small changes in height due to the mm-scale thickness of compliant tissue samples, and this prestrain/prestress has been shown to considerably increase the measured shear moduli of brain tissue [51]. Shear rheology is also limited by a maximum measurable frequency due to instrument limitations such as frame inertia upon reversal of shearing displacement. Moreover, the rheology models used to analyze the brain tissue response assume the material to be homogenous and isotropic material properties, a simplifying idealization that does not hold strictly for brain tissue (or most biological soft tissues).

For each deformation length scale and method, we recognized these limitations and simplifications that would affect the accuracy of the magnitude of extracted mechanical properties, and thus designed our experiments to enable systematic comparisons of a given property between two sample groups: brain tissue obtained from control and TSC cohorts. In fact, Table 1 illustrates that the magnitude of a given property can vary with measurement approach; such differences are attributed reasonably to each method's deviation from all assumptions employed in data analysis and potentially to actual differences at different length scales and deformation rates. However, we emphasize that our goal herein was to consider detectable and significant differences in any one property, measured in the same way and under the same conditions, between murine brain tissue with and without this TSC genetic mutation associated with ASD.

The various limitations for each characterization technique, along with the inherent interregional and sample-to-sample variation of brain tissue, can contribute to the standard deviation of properties reported in Figs. 1–3, as one consideration of measurement precision. This variation can potentially obfuscate resolution of any differences in mechanical properties between control and TSC brain tissue. However, the number of replicate measurements, replicate samples, and independent experiments for each approach provides confidence that these mechanical properties do not differ among mouse brain tissue obtained from the control and TSC cohorts. While this finding is clear for this animal model, our findings neither demonstrate nor do we suggest that brain tissue of humans exhibiting autism spectrum disorder are mechanically indistinguishable from brain tissue of those who do not exhibit such characteristics. One key feature of human brain, not shared by murine brain, is that it undergoes gyrification. Previous studies have associated abnormalities in brain folding with autism [71–73], and thus that distinction remains a topic of important future consideration that can draw on the approaches and findings discussed herein.

5 Conclusion

Despite structural changes of the cellular components in our TSC/ASD mouse brain model, such as hypomyelination and disorganization of axons, we found that tissue mechanical properties were unaffected at every length- and time-scale explored. Stiffness of neuronal axons transfected with *Tsc1* knockout was also unaffected in ways that could be correlated with this mutation. We found the expression levels of fibronectin in TSC and control brain tissue to be similar, which is consistent with the lack of mechanical differences observed. Our results indicate that cell-level changes in myelination and neuronal organization do not manifest in detectable mechanical changes for this particular murine model of ASD. Future work can leverage these methods to determine whether other genetic or animal models that are related to autism spectrum disorder result in mechanical changes that may serve as cues to promote or sustain the cell-level responses associated with ASD.

Acknowledgment

This research was supported by the National Multiple Sclerosis Society and Simons Center for the Social Brain. B. Q. gratefully acknowledges support from the U.S. National Defense Science & Engineering Graduate Fellowship.

References

[1] Curatolo, P., Bombardieri, R., and Jozwiak, S., 2008, "Tuberous Sclerosis," Lancet, **372**(9639), pp. 657–668.

[2] Jeste, S. S., Sahin, M., Bolton, P., Ploubidis, G. B., and Humphrey, A., 2008, "Characterization of Autism in Young Children With Tuberous Sclerosis Complex," J. Child Neurol., **23**(5), pp. 520–525.

[3] Tsai, P., and Sahin, M., 2011, "Mechanisms of Neurocognitive Dysfunction and Therapeutic Considerations in Tuberous Sclerosis Complex," Curr. Opin. Neurol., **24**(2), pp. 106–113.

[4] Meikle, L., Talos, D. M., Onda, H., Pollizzi, K., Rotenberg, A., Sahin, M., Jensen, F. E., and Kwiatkowski, D. J., 2007, "A Mouse Model of Tuberous Sclerosis: Neuronal Loss of Tsc1 Causes Dysplastic and Ectopic Neurons, Reduced Myelination, Seizure Activity, and Limited Survival," J. Neurosci., **27**(21), pp. 5546–5558.

[5] Meikle, L., Pollizzi, K., Egnor, A., Kramvis, I., Lane, H., Sahin, M., and Kwiatkowski, D. J., 2008, "Response of a Neuronal Model of Tuberous Sclerosis to Mammalian Target of Rapamycin (mTOR) Inhibitors: Effects on mTORC1 and Akt Signaling Lead to Improved Survival and Function," J. Neurosci., **28**(21), pp. 5422–5432.

[6] Choi, Y., Di Nardo, A., Kramvis, I., Meikle, L., Kwiatkowski, D. J., Sahin, M., and He, X., 2008, "Tuberous Sclerosis Complex Proteins Control Axon Formation," Genes Develop., **22**(18), pp. 2485–2495.

[7] Nie, D., Di Nardo, A., Han, J. M., Baharanyi, H., Kramvis, I., Huynh, T., Dabora, S., Codeluppi, S., Pandolfi, P., Pasquale, E., and Sahin, M., 2010, "TSC2-Rheb Signaling Regulates EphA-Mediated Axon Guidance," Nat. Neurosci., **13**(2), pp. 163–172.

[8] Lewis, W. W., Sahin, M., Scherrer, B., Peters, J. M., Suarez, R. O., Vogel-Farley, V. K., Jeste, S. S., Gregas, M. C., Prabhu, S. P., Nelson, C. A., and Warfield, S. K., 2013, "Impaired Language Pathways in Tuberous Sclerosis Complex Patients With Autism Spectrum Disorders," Cere. Cortex, **23**(7), pp. 1526–1532.

[9] Peters, J. M., Sahin, M., Vogel-Farley, V. K., Jeste, S. S., Nelson, C. A., Gregas, M. C., Prabhu, S. P., Scherrer, B., and Warfield, S. K., 2012, "Loss of White Matter Microstructural Integrity is Associated With Adverse Neurological Outcome in Tuberous Sclerosis Complex," Acad. Radiol., **19**(1), pp. 17–25.

[10] Tillema, J. M., Leach, J. L., Krueger, D. A., and Franz, D. N., 2012, "Everolimus Alters White Matter Diffusion in Tuberous Sclerosis Complex," Neurology, **78**(8), pp. 526–531.

[11] van Dommelen, J. A. W., Hrapko, M., and Peters, G. W. M., 2009, "Mechanical Properties of Brain Tissue: Characterisation and Constitutive Modelling," *Mechanosensitivity of the Nervous System* (Mechanosensitivity in Cells and Tissues, Vol. 2), A. Kamkim and I. Kiseleva, eds., Springer, Berlin, pp. 249–279.

[12] Ingber, D. E., 2003, "Mechanobiology and Diseases of Mechanotransduction," Ann. Med., **35**(8), pp. 564–577.

[13] Murphy, M. C., Huston, J., Jack, C. R., Glaser, K. J., Manduca, A., Felmlee, J. P., and Ehman, R. L., 2012, "Decreased Brain Stiffness in Alzheimer's Disease Determined by Magnetic Resonance Elastography," J. Magn. Reson. Imaging, **34**(3), pp. 494–498.

[14] Wuerfel, J., Paul, F., Beierbach, B., Hamhaber, U., Klatt, D., Papazoglou, S., Zipp, F., Martus, P., Braun, J., and Sack, I., 2010, "MR-Elastography Reveals Degradation of Tissue Integrity in Multiple Sclerosis," NeuroImage, **49**(3), pp. 2520–2525.

[15] Riek, K., Millward, J. M., Hamann, I., Mueller, S., Pfueller, C. F., Paul, F., Braun, J., Infante-Duarte, C., and Sack, I., 2012, "Magnetic Resonance Elastography Reveals Altered Brain Viscoelasticity in Experimental Autoimmune Encephalomyelitis," NeuroImage. Clin., **1**(1), pp. 81–90.

[16] Liu, F., and Tschumperlin, D. J., 2011, "Micro-Mechanical Characterization of Lung Tissue Using Atomic Force Microscopy," J. Visualized Exp., (54), p. e2911.

[17] Peaucelle, A., 2014, "AFM-Based Mapping of the Elastic Properties of Cell Walls: At Tissue, Cellular, and Subcellular Resolutions," J. Visualized Exp., (89), p. e51317.

[18] Thomas, G., Burnham, N. A., Camesano, T. A., and Wen, Q., 2013, “Measuring the Mechanical Properties of Living Cells Using Atomic Force Microscopy,” J. Visualized Exp., (76), p. e50497.

[19] Moreno-Flores, S., Benitez, R., Vivanco, M. D., and Toca-Herrera, J. L., 2010, “Stress Relaxation and Creep on Living Cells With the Atomic Force Microscope: A Means to Calculate Elastic Moduli and Viscosities of Cell Components,” Nanotechnology, **21**(44), p. 445101.

[20] Moreno-Flores, S., Benitez, R., Vivanco, M. D., and Toca-Herrera, J. L., 2010, “Stress Relaxation Microscopy: Imaging Local Stress in Cells,” J. Biomech., **43**(2), pp. 349–354.

[21] Desprat, N., Richert, A., Simeon, J., and Asnacios, A., 2005, “Creep Function of a Single Living Cell,” Biophys. J., **88**(3), pp. 2224–2233.

[22] Lu, H., Wang, B., Ma, J., Huang, G., and Viswanathan, H., 2003, “Measurement of Creep Compliance of Solid Polymers by Nanoindentation,” Mech. Time-Dependent Mater., **7**(3/4), pp. 189–207.

[23] Cheng, L., Xia, X., Scriven, L. E., and Gerberich, W. W., 2005, “Spherical-Tip Indentation of Viscoelastic Material,” Mech. Mater., **37**(1), pp. 213–226.

[24] Kalcioglu, Z., Qu, M., and Van Vliet, 2010, “Multiscale Characterization of Relaxation Times of Tissue Surrogate Gels and Soft Tissues,” Seventh Army Science Conference.

[25] Zhu, Y., Romero, M. I., Ghosh, P., Ye, Z., Charnay, P., Rushing, E. J., Marth, J. D., and Parada, L. F., 2001, “Ablation of NF1 Function in Neurons Induces Abnormal Development of Cerebral Cortex and Reactive Gliosis in the Brain,” Genes Develop., **15**(7), pp. 859–876.

[26] Batra, R. C., and Jiang, W., 2008, “Analytical Solution of the Contact Problem of a Rigid Indenter an Anisotropic Linear Elastic Layer,” Int. J. Solids Struct., **45**(22–23), pp. 5814–5830.

[27] Argatov, I. I., 2011, “Depth-Sensing Indentation of a Transversely Isotropic Elastic Layer: Second-Order Asymptotic Models for Conical Indenters,” Int. J. Solids Struct., **48**(25–26), pp. 3444–3452.

[28] Britton, T. B., Liang, H., Dunne, F. P. E., and Wilkinson, A. J., 2010, “The Effect of Crystal Orientation on the Indentation Response of Commercially Pure Titanium: Experiments and Simulations,” Proc. R. Soc. A, **466**(2115), pp. 695–719.

[29] Moeendarbary, E., Weber, I. P., Sheridan, G. K., Koser, D. E., Soleman, S., Haenzi, B., Bradbury, E. J., Fawcett, J., and Franze, K., 2017, “The Soft Mechanical Signature of Glial Scars in the Central Nervous System,” Nat. Commun., **8**, p. 14787.

[30] Canovic, E. P., Qing, B., Mijailovic, A. S., Jagielska, A., Whitfield, M. J., Kelly, E., Turner, D., Sahin, M., and Van Vliet, K. J., 2016, “Characterizing Multiscale Viscoelastic Properties of Brain Tissue Using Atomic Force Microscopy, Impact Indentation, and Rheometry,” J. Visualized Exp., (115), p. e54201.

[31] Lin, D. C., Dimitriadis, E. K., and Horkay, F., 2007, “Robust Strategies for Automated AFM Force Curve Analysis-II: Adhesion-Influenced Indentation of Soft, Elastic Materials,” ASME J. Biomech. Eng., **129**(6), pp. 904–912.

[32] Oliver, W. C., and Pharr, G. M., 2004, “Measurement of Hardness and Elastic Modulus by Instrumented Indentation: Advances in Understanding and Refinements to Methodology,” J. Mater. Res., **19**(1), pp. 3–20.

[33] Herbert, E., Pharr, G. M., Oliver, W. C., Lucas, B. N., and Hay, J. L., 2001, “On the Measurement of Stress–Strain Curves by Spherical Indentation,” Thin Solid Films, **398–399**, pp. 331–335.

[34] Lee, E. H., and Radok, J. R. M., 1960, “The Contact Problem for Viscoelastic Bodies,” ASME J. Appl. Mech., **27**(3), pp. 438–444.

[35] Lakes, R. S., and Wineman, A., 2006, “On Poisson’s Ratio in Linearly Viscoelastic Solids,” J. Elasticity, **85**(1), pp. 45–63.

[36] Samadi-dooki, A., Voyiadjis, G. Z., and Stout, R. W., 2018, “A Combined Experimental, Modeling, and Computational Approach to Interpret the Viscoelastic Response of White Matter Brain Tissue During Indentation,” J. Mech. Behav. Biomed. Mater., **77**, pp. 24–33.

[37] Janmey, P. A., Georges, P. C., and Hvidt, S., 2007, “Basic Rheology for Biologists,” Methods Cell Biol., **83**, pp. 3–27.

[38] Mijailovic, A. S., Qing, B., Fortunato, D., and Van Vliet, K. J., 2018, “Characterizing Viscoelastic Mechanical Properties of Highly Compliant Polymers and Biological Tissues Using Impact Indentation,” Acta Biomater., **71**, pp. 388–397.

[39] MacManus, D. B., Pierrat, B., Murphy, J. G., and Gilchrist, M. D., 2017, “Region and Species Dependent Mechanical Properties of Adolescent and Young Adult Brain Tissue,” Sci. Rep., **7**, p. 13729.

[40] Rashid, B., Destrade, M., and Gilchrist, M. D., 2012, “Mechanical Characterization of Brain Tissue in Compression at Dynamic Strain Rates,” J. Mech. Behav. Biomed. Mater., **10**, pp. 23–38.

[41] Weickenmeier, J., de Rooji, R., Budday, S., Steinmann, P., Ovaert, T. C., and Kuhl, E., 2016, “Brain Stiffness Increases With Myelin Content,” Acta Biomater., **42**, pp. 265–272.

[42] Budday, S., Nay, R., de Rooji, R., Steinmann, P., Wyrobek, T., Ovaert, T. C., and Kuhl, E., 2015, “Mechanical Properties of Gray and White Matter Brain Tissue by Indentation,” J. Mech. Behav. Biomed. Mater., **46**, pp. 318–330.

[43] Kalcioglu, Z. I., Qu, M., Strawhecker, K. E., Shazly, T., Edelman, E., VanLandingham, M. R., Smith, J. F., and Van Vliet, K. J., 2011, “Dynamic Impact Indentation of Hydrated Biological Tissues and Tissue Surrogate Gels,” Philos. Mag., **91**(7–9), pp. 1339–1355.

[44] Qing, B., and Van Vliet, K. J., 2016, “Hierarchical Design of Synthetic Gel Composites Optimized to Mimic the Impact Energy Dissipation of Brain Tissue,” Mol. Syst. Des. Eng., **1**(3), pp. 290–300.

[45] Finan, J. D., Fox, P. M., and Morrison, B., III, 2014, “Non-Ideal Effects in Indentation Testing of Soft Tissues,” Biomech. Model. Mechanobiol., **13**(3), pp. 573–584.

[46] Constantinides, G., Kalcioglu, Z. I., McFarland, M., Smith, J. F., and Van Vliet, K. J., 2008, “Probing Mechanical Properties of Fully Hydrated Gels and Biological Tissues,” J. Biomech., **41**(15), pp. 3285–3289.

[47] Nicolle, S., Lounis, M., and Willinger, R., 2004, “Shear Properties of Brain Tissue Over a Frequency Range Relevant for Automotive Impact Situations: New Experimental Results,” Stapp Car Crash J., **48**, pp. 239–258.

[48] Hrapko, M., van Dommelen, J. A., Peters, G. W., and Wismans, J. S., 2006, “The Mechanical Behaviour of Brain Tissue: Large Strain Response and Constitutive Modelling,” Biorheology, **43**(5), pp. 623–636.

[49] Kalcioglu, Z. I., Mrozek, R., Mahmoodian, R., VanLandingham, M. R., Lenhart, J. L., and Van Vliet, K. J., 2013, “Tunable Mechanical Behavior of Synthetic Organogels as Biofidelic Tissue Simulants,” J. Biomech., **46**(9), pp. 1583–1591.

[50] Shen, F., Tay, T. E., Li, J. Z., Nigen, S., Lee, P. V., and Chan, H. K., 2006, “Modified Bilston Nonlinear Viscoelastic Model for Finite Element Head Injury Studies,” ASME J. Biomech. Eng., **128**(5), pp. 797–801.

[51] Pogoda, K., Chin, L., Georges, P. C., Byfield, F. J., Bucki, R., Kim, R., Weaver, M., Wells, R. G., Marcinkiewicz, C., and Janmey, P. A., 2014, “Compression Stiffening of Brain and Its Effect on Mechanosensing by Glioma Cells,” New J. Phys., **16**(7), p. 075002.

[52] Stoffels, J. M., de Jonge, J. C., Stancic, M., Nomden, A., van Strien, M. E., Ma, D., Siskova, Z., Maier, O., Ffrench-Constant, C., Franklin, R. J., Hoekstra, D., Zhao, C., and Baron, W., 2013, “Fibronectin Aggregation in Multiple Sclerosis Lesions Impairs Remyelination,” Brain, **136**(1), pp. 116–131.

[53] Milner, R., Crocker, S. J., Hung, S., Wang, X., Frausto, R. F., and del Zoppor, G. J., 2007, “Fibronectin- and Vitronectin-Induced Microglial Activation and Matrix Metalloproteinase-9 Expression Is Mediated by Integrins $\alpha_5\beta_1$ and $\alpha_v\beta_5$,” J. Immunol., **178**(12), pp. 8158–8167.

[54] Schregel, K., Wuerfel, E., Garteiser, P., Gemeinhardt, I., Prozorovski, T., Aktas, O., Merz, H., Petersen, D., Wuerfel, J., and Sinkus, R., 2012, “Demyelination Reduces Brain Parenchymal Stiffness Quantified In Vivo by Magnetic Resonance Elastography,” Proc. Natl. Acad. Sci. U.S.A., **109**(17), pp. 6650–6655.

[55] Uysal, H., and Hemming, F. W., 1999, “Changes in the Expression and Distribution of Fibronectin, Laminin and Tenascin by Cultured Fibroblasts From Skin Lesions of Patients With Tuberous Scleroris,” Br. J. Dermatol., **141**(4), pp. 658–666.

[56] Weickenmeier, J., de Rooji, R., Budday, S., Ovaert, T. C., and Kuhl, E., 2017, “The Mechanical Importance of Myelination in the Central Nervous System,” J. Mech. Behav. Biomed. Mater., **76**, pp. 119–124.

[57] Bush, E. C., and Allman, J. M., 2003, “The Scaling of White Matter to Gray Matter in Cerebellum and Neocortex,” Brain, Behav. Evol., **61**(1), pp. 1–5.

[58] Finan, J. D., Pearson, E. M., and Morrison, B., III, 2012, “Viscoelastic Properties of the Rat Brain in the Horizontal Plane,” IRCOBI Conference, Dublin, Ireland, Sept. 12–14, pp. 474–485.

[59] Yoganandan, N., Pintar, F. A., Stemper, B. D., Schlick, M. B., Philippens, M., and Wismans, J., 2000, “Biomechanics of Human Occupants in Simulated Rear Crashes: Documentation of Neck Injuries and Comparison of Injury Criteria,” Stapp Car Crash J., **44**, pp. 189–204.

[60] Hrapko, M., van Dommelen, J. A., Peters, G. W., and Wismans, J. S., 2008, “Characterisation of the Mechanical Behaviour of Brain Tissue in Compression and Shear,” Biorheology, **45**(6), pp. 663–676.

[61] Feng, Y., Okamoto, R. J., Namani, R., Genin, G. M., and Bayly, P. V., 2013, “Measurements of Mechanical Anisotropy in Brain Tissue and Implications for Transversely Isotropic Material Models of White Matter,” J. Mech. Behav. Biomed. Mater., **23**, pp. 117–132.

[62] Franze, K., Janmey, P. A., and Guck, J., 2013, “Mechanics in Neuronal Development and Repair,” Annu. Rev. Biomed. Eng., **15**(1), pp. 227–251.

[63] van Horssen, J., Dijkstra, C. D., and de Vries, H. E., 2007, “The Extracellular Matrix in Multiple Sclerosis Pathology,” J. Neurochem., **103**(4), pp. 1293–301.

[64] Bonneh-Barkay, D., and Wiley, C. A., 2009, “Brain Extracellular Matrix in Neurodegeneration,” Brain Pathol., **19**(4), pp. 573–585.

[65] Dityatev, A., Seidenbecher, C. I., and Schachner, M., 2010, “Compartmentalization From the Outside: The Extracellular Matrix and Functional Microdomains in the Brain,” Trends Neurosci., **33**(11), pp. 503–512.

[66] Chatelin, S., Constantinesco, A., and Willinger, R., 2010, “Fifty Years of Brain Tissue Mechanical Testing: From In Vitro to In Vivo Investigations,” Biorheology, **47**(5–6), pp. 255–276.

[67] van Dommelen, J. A., van der Sande, T. P., Hrapko, M., and Peters, G. W., 2010, “Mechanical Properties of Brain Tissue by Indentation: Interregional Variation,” J. Mech. Behav. Biomed. Mater., **3**(2), pp. 158–166.

[68] Elkin, B. S., Ilankovan, A., and Morrison, B., 2010, “Age-Dependent Regional Mechanical Properties of the Rat Hippocampus and Cortex,” ASME J. Biomech. Eng., **132**(1), p. 011010.

[69] Jagielska, A., Norman, A. L., Whyte, G., Van Vliet, K. J., Guck, J., and Franklin, R. J., 2012, “Mechanical Microenvironment Modulates Biological Properties of Oligodendrocyte Progenitor Cells,” Stem Cells Develop., **21**(16), pp. 2905–2914.

[70] Van Vliet, K. J., 2010, “Instrumentation and Experimentation,” *Handbook of Nanoindentation*, M. Oyen, ed., Pan Stanford, New York, p. 39.

[71] Hardan, A. Y., Jou, R. J., Keshavan, M. S., Varma, R., and Minshew, N. J., 2004, “Increased Frontal Cortical Folding in Austim; A Preliminary MRI Study,” Psychiatr. Res., **131**(3), pp. 263–268.

[72] Nordahl, C. W., Dierker, D., Mostafavi, I., Schumann, C. M., Rivera, S. M., Amaral, D. G., and Van Essen, D. C., 2007, “Cortical Folding Abnormalities in Autism Revealed by Surface-Based Morphometry,” J. Neurosci., **27**(43), pp. 11725–11735.

[73] Budday, S., Steinmann, P., and Kuhl, E., 2015, “Physical Biology of Human Brain Development,” Front. Cellular Neurosci., **9**, p. 257.